Prompt-Guided Zero-Shot Depth-Aware Transformer Pipeline for Democratized SEM Particle Characterization: A Case Study in Battery Materials

Ahmed Eisa[1*], Mayank Gupta[2], Alex Kong[3], Finn Frankenberg[1], Maximilian Kissel[4], Dimitri Ivanov[1], Kostas Giannis[1] and Carsten Schilde[1]

[1*] Institute for Particle Technology, Technical University of Braunschweig, Volkmaroder Str. 5, Brunswick, 38108, Lower Saxony, Germany.
ahmed.eisa@tu-braunschweig.de; finn.frankenberg@tu-braunschweig.de; d.ivanov@tu-braunschweig.de; k.giannis@tu-braunschweig.de;c.schilde@tu-braunschweig.de

[2] Indian Institute of Technology Bombay, Academic Section, IIT Area, Mumbai, 400076, Maharashtra, India.
210101002@iitb.ac.in

[3] University of Quebec in Outaouais, 283 Alexandre-Taché Blvd, Quebec J8X 3X7, Canada.
kona39@uqo.ca

[4] Justus Liebig University Gießen, Ludwigstraße 23, 35390 Gießen, Germany.
maximilian.kissel@pc.jlug.de

Abstract. Particle characterization remains challenging for complex samples with overlapping particles, agglomerates, and heterogeneous surfaces. This work integrates transformer-based foundation models, the segment anything model (SAM) for segmentation and dense prediction transformers for depth estimation to enable comprehensive, domain-agnostic analysis of particle size, shape, and surface roughness. Validation on aluminum oxide samples demonstrated clear superiority over conventional methods: OpenCV failed to segment overlaps, while Cellpose overestimated particle sizes by 25–100%. Despite analyzing only ~0.1% of the population, the pipeline closely matched QICPIC reference data (~950,000 particles) with D_{50} deviations of 5.5–17%. A novel interactive prompt guided segmentation system leveraging SAM's capabilities enables expert-guided segmentation of complex, multi-component samples. A novel depth-based roughness characterization system for particle surface roughness estimation achieved moderate correlation with profile methods ($r \approx 0.64$) despite scaling offsets. Applied to solid-state battery materials, the method resolved submicron primary particles (D_{50} = 0.54µm) within agglomerates measured at 9.47µm, a 17.5× discrepancy critical for electrode design. By leveraging foundation models, this work introduces an accessible, generalizable pipeline that democratizes advanced particle characterization through an interactive Python based implementation.

Keywords: Particle characterization, Particle Surface roughness, Foundation models, Zero-shot learning, Depth Analysis, Interactive segmentation, Solid-state batteries

1 Introduction

Particle characterization faces fundamental limitations when analyzing complex samples with overlapping particles, agglomerates, and heterogeneous surfaces. Traditional measurement approaches including laser diffraction, sieve analysis, and optical microscopy provide quantitative assessment of particle size distributions and morphological properties [1,2,3], yet encounter significant constraints when distinguishing primary particles from agglomerates and analyzing samples with complex morphologies [4,5,6].

Computer vision approaches have emerged as alternatives, enabling direct morphological characterization from microscopy images [7,8]. Traditional image processing methods employ classical algorithms including mathematical morphology [9,10], threshold-based segmentation [11], and edge detection [12] to identify particle boundaries. Watershed segmentation [13] and morphological operations [14] have been adopted for separating touching particles, yet these approaches struggle with complex particle arrangements and varying imaging conditions.

Deep learning has transformed image analysis across multiple domains [15,16]. Convolutional neural networks, particularly U-Net architectures [17], have demonstrated success in biomedical image segmentation. Instance segmentation methods such as Mask R-CNN [18] enable simultaneous object detection and precise boundary delineation. Specialized networks including U-Net variants [19] and nucleus segmentation algorithms [20] have been developed for microscopy applications. Cellpose represents an advancement as a generalist algorithm for cellular segmentation [21], trained on diverse microscopy datasets to achieve performance across different cell types and imaging modalities. Despite these advances, deep learning approaches for particle characterization typically require substantial domain-specific training datasets and struggle with generalization across different particle systems, imaging conditions, and preparation protocols [22,23]. Transfer learning techniques [24,25] can partially address these limitations, but domain adaptation remains challenging for specialized applications.

Foundation models represent a paradigm shift in artificial intelligence, offering capabilities for zero-shot task performance across diverse domains [26]. Vision-language models such as CLIP [27] demonstrate cross-modal understanding, while the segment anything model (SAM) [28] has established benchmarks for zero-shot image segmentation. Built on transformer architectures [29] and Vision Transformer (ViT) backbones [30], these models leverage massive-scale pretraining to develop generalizable visual understanding that transfers to specialized scientific applications.

Surface roughness characterization represents another critical dimension of particle analysis, traditionally requiring specialized instrumentation such as atomic force microscopy (AFM) or stylus profilometry [31,32]. AFM provides nanometer-scale resolution for surface topography measurements [33,34] but is limited to small sample areas

and requires complex sample preparation and expert operation [35,36]. Alternative approaches based on fractal analysis [37] offer mathematical frameworks for surface characterization but lack direct physical interpretation.

Monocular depth estimation has emerged as a computer vision technique enabling 3D scene reconstruction from single images [38]. Self-supervised approaches [39] and transformer-based architectures [40] have achieved accuracy in depth prediction tasks. dense prediction transformers (DPT) [41] represent models for monocular depth estimation, trained on diverse datasets [42] to develop understanding of geometric relationships and photometric cues [43]. These models demonstrate zero-shot generalization across different domains, making them potentially valuable for scientific imaging applications.

Recent advances in deep learning have extended to semantic segmentation applications [44,45], with fully convolutional networks and DeepLab architectures establishing baselines for dense prediction tasks. Surface texture analysis benefits from standardized protocols including ISO 4287 and ISO 4288 [46,47] for roughness quantification, while dynamic image analysis systems such as QICPIC [48,49] provide reference standards for particle size and shape measurements according to ISO 13322-2 guidelines. Computer vision libraries including OpenCV [50] enable implementation of traditional image processing algorithms for comparative evaluation.

Solid-state batteries represent a critical application domain where precise particle characterization is essential for performance optimization [51,52]. The microstructure of composite cathodes, particularly the particle size distribution (PSD) of active materials and solid electrolytes, directly influences ionic conductivity, mechanical stability, and electrochemical performance. Conventional characterization methods face challenges in this domain where laser diffraction measures agglomerates rather than primary particles, wet dispersion methods require inert solvents that may alter material properties, and the air-sensitivity of many solid electrolytes precludes traditional sample preparation approaches.

Established standards for particle characterization include ISO 13322-1 for static image analysis [53] and ISO 9276-6 for shape and morphology representation [54], while statistical analysis follows protocols such as DIN 66141 for grain size distribution representation [55]. These standardized approaches provide frameworks for quantitative particle analysis but require adaptation for emerging measurement technologies and complex particle systems. We address these fundamental limitations through novel integration of transformer-based foundation models with specialized algorithms for materials analysis. Our comprehensive pipeline combines the SAM for zero-shot particle segmentation with DPT for depth-aware surface roughness analysis, enabling advanced characterization capabilities without domain-specific training requirements.

We demonstrate a comprehensive application of the SAM for multi-scale particle analysis, achieving better performance compared to conventional computer vision and

specialized microscopy models like cellpose on complex samples. This transformer-based segmentation system eliminates the need for domain-specific training while maintaining high accuracy across diverse particle systems and imaging conditions. We extend SAM's interactive prompting using point clicks, bounding boxes, and mask sketching to particle characterization, enabling interactive prompt guided segmentation system (IPGSS) in complex multi-component samples.

We further introduce the first hemisphere-scale depth-based roughness characterization system (DRCS) from standard Scanning Electron Microscope (SEM) images via zero-shot depth estimation, capturing approximately half of each particle's surface area compared to the localized regions accessible by AFM, while eliminating the need for specialized instrumentation. Extensive validation spans three domains: (1) size and shape comparison against QICPIC reference measurements from ~950,000 particles, (2) surface roughness validation against AFM validated profile-based method results on nine core–shell microparticles, and (3) practical demonstration on solid-state battery (SSB) materials resolving submicron primary particles within agglomerates.

A hierarchical filtering strategy combining transformer confidence scoring with microscopy-specific algorithms ensures measurement reliability and ISO compliance. Finally, we provide an open-source Python implementation with interactive segmentation tools, enabling guided accurate particle characterization for microscopy datasets. The pipeline architecture integrating these components is illustrated in Figure 1, showing a simplified workflow from microscopy input through transformer-based analysis to quantitative characterization outputs.

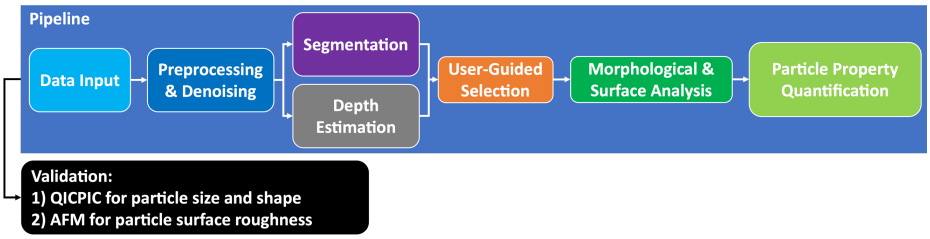

Fig. 1. Pipeline architecture for transformer-based particle characterization. The workflow includes preprocessing, segmentation with depth estimation, user-guided selection, and morphological and surface analysis for final property quantification. Validation is performed using QICPIC for size and shape and AFM validated contour-based profile method data for surface roughness.

2 Methodology

2.1 Sample Preparation and Experimental Setup

Size and Shape Validation Materials. For validation, aluminum oxide samples (Final GmbH, Noxid Pulver-160, 99.8% purity, $D_{50} \approx 50\mu m$) were prepared under two conditions to evaluate the segmentation system's performance across preparation protocols. In the dry condition (2-D), powder was gently spread on glass slides to form a monolayer or near-monolayer, minimizing preferential orientation effects. Excess material was removed by controlled tapping, yielding representative PSDs suitable for optical microscopy. In the dispersed condition (2-Di), samples were ultrasonicated in water for 5 minutes at room temperature using standardized power settings to ensure reproducible dispersion without particle fracture. Suspensions were deposited by calibrated micropipette drop-casting. High-resolution optical images were acquired with a WITec alpha300 R microscope under standardized settings: consistent illumination, fixed working distance, calibrated white balance, and per-field focus adjustment (Figure 2, left).

Reference distributions were obtained with a QICPIC dynamic image analysis system (Sympatec, Germany) operated according to ISO 13322-2. Each condition involved ~950,000 particles, providing statistically robust ground truth. QICPIC employed high-speed imaging with stroboscopic illumination to capture particles in motion under both dispersed and dry measurement conditions, ensuring reliable detection across preparation modes (Figure 2, middle). Sample preparation protocols for both conditions are illustrated in Figure 2, right. The dry measurement required a noticeably larger sample volume than the dispersed condition to maintain stable material feed and consistent particle flow through the QICPIC system. Each condition was measured multiple times to ensure measurement stability and accuracy. While QICPIC provides large-population reference measurements, it has practical limitations: it requires comparatively large sample quantities, which is problematic when working with expensive or scarce materials, and sample handling becomes more difficult for toxic, reactive, or air-sensitive powders that may interact unfavorably with the QICPIC dispersion environment. In contrast, microscopy-based analysis combined with SAM requires only minute sample amounts, avoids potentially reactive dispersion steps, and remains compatible with hazardous or sensitive materials providing a more flexible and accessible characterization option.

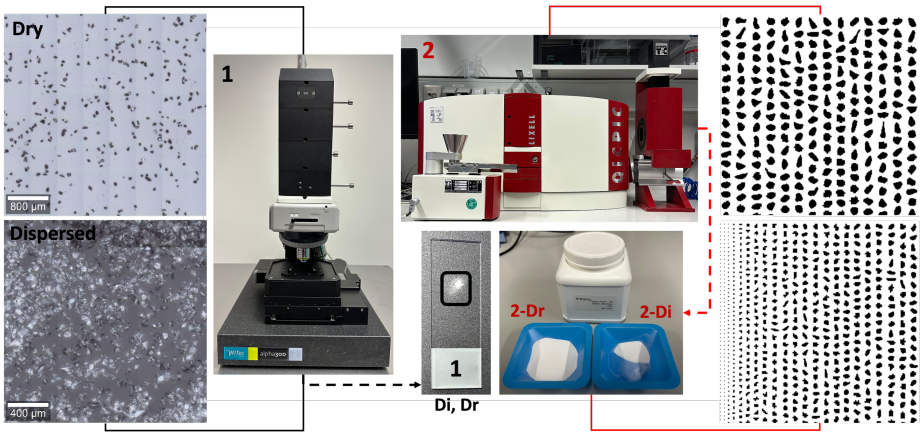

Fig. 2. Experimental setup for particle size and shape validation. Optical microscopy (WITec alpha300 R) and dynamic image analysis (QICPIC) were used in parallel, with samples prepared under dry powder (2-Dr) and dispersed suspension (2-Di) conditions to evaluate consistency across measurement modalities.

Surface Roughness Validation Dataset. For validation, nine particles were selected from the open-source dataset of Hülagü et al. [36]. The dataset contains high-resolution SEM images together with AFM-validated, profile-based roughness measurements of of PS/Fe_3O_4 and PS/Fe_3O_4/SiO_2 core–shells microparticles synthesized under controlled conditions to yield systematic variations in surface roughness.

Validation was performed on nine particles selected to span a broad range of architectural complexity and surface morphology. Particles 1 and 2**,** corresponding to the material type PS/Fe_3O_4**,** exhibit a core–shell structure with comparatively low surface complexity. The remaining Particles 3–9 correspond to the material type PS/Fe_3O_4/SiO_2 and were drawn from two synthesis batches: Batch 1 includes Particles 3, 4, 6, and 7, while Batch 2 includes Particles 5, 8, and 9. Together, these samples capture a wide range of surface complexities, with representative images shown in Figure 3 (top).

The dataset provides validated ground-truth measurements through two complementary methodologies operating at different spatial scales. The contour-based profile method, which is used in this work in its AFM-validated form, extracts roughness from 2D particle-boundary fluctuations analyzed from multiple viewing angles, capturing edge irregularities that correspond to surface features intersecting the particle silhouette (Figure 3, bottom right). AFM measurements provide direct 3D topographical analysis of highly localized surface regions representing only a fraction of the total particle surface but offer nanometer-scale height resolution for detailed characterization (Figure 3, bottom left).

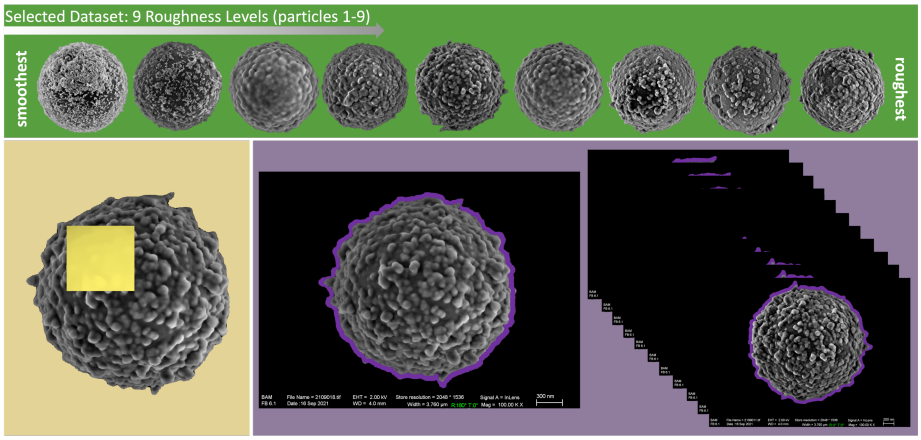

Fig. 3. Surface roughness validation framework based on the validation dataset. (top) Representative SEM images of the validation particles (1-9) spanning nine roughness levels. (bottom left) AFM scans visualization example on particle 5 providing 3D topography ground truth. (bottom right) Contour-based profile analysis method visualization example, extracting boundary fluctuations as a roughness measure.

2.2 Interactive Particle Segmentation Using SAM

Zero-Shot Segmentation System Implementation. SAM serves as the core segmentation engine, implementing a ViT-H/16 vision transformer trained on the SA-1B dataset (>1 billion masks across 11 million images). This large-scale pretraining enables robust zero-shot generalization to particle microscopy despite the domain shift from natural to scientific imagery. The transformer architecture departs from traditional segmentation by using self-attention to capture global context and long-range dependencies, allowing accurate boundary detection in complex particle arrangements. Through extensive pretraining, SAM develops generalizable visual concepts that transfer effectively to microscopy without domain-specific datasets, maintaining high segmentation accuracy. Although SAM does not implement formal probabilistic uncertainty quantification, it outputs multiple candidate masks for each prompt along with predicted IoU confidence scores, which serve as a practical proxy for uncertainty. A built-in stability score further evaluates mask robustness under threshold variations, enabling the rejection of low-confidence or ambiguous boundaries.

The image encoder processes inputs resized so that the longest side is 1024 px and padded to a 1024 × 1024 tensor, producing dense feature maps that preserve both local detail and global context. User prompts are converted to embeddings by the prompt encoder, guiding the lightweight mask decoder to produce real-time outputs. The complete workflow (Figure 4) begins with calibrated microscopy images, followed by segmentation in either automatic batch mode or interactive prompting. Outputs are refined using a four-stage hierarchical filtering cascade and subsequently quantified through

seven geometric and morphological parameters, with percentile-based distributions reported in line with commercial standards.

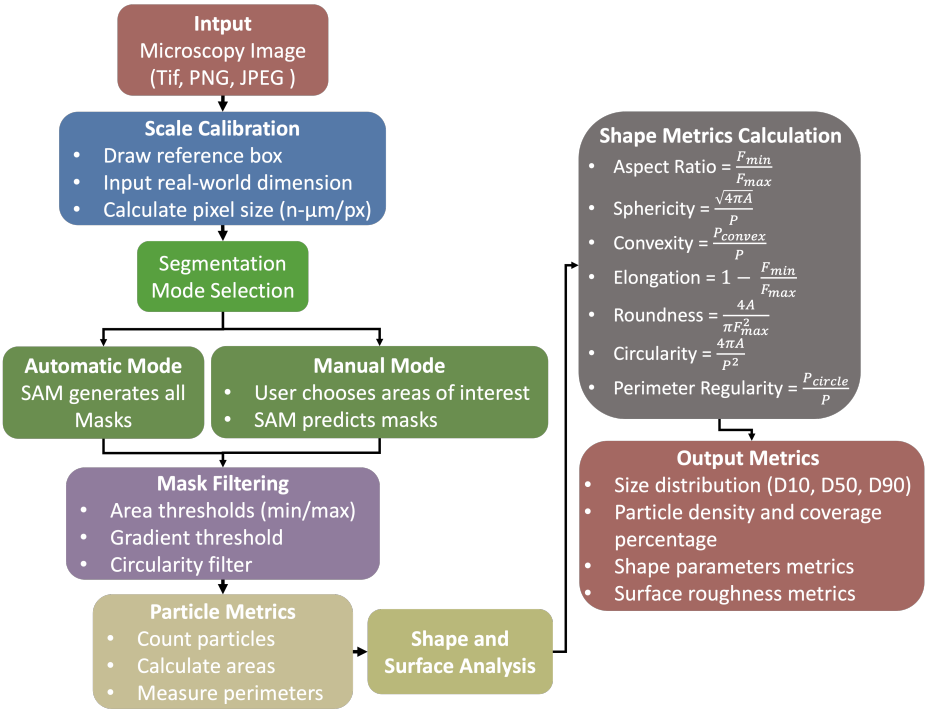

Fig. 4. Workflow for particle shape analysis integrating SAM-based segmentation with spatial calibration, mask filtering, and morphological parameter calculation. The segmentation system supports both automatic and manual segmentation modes, followed by shape and surface metric extraction and statistical analysis to generate QICPIC-compatible outputs.

Dual-Mode Segmentation System. The developed system supports two complementary modes. Automatic mode exploits SAM's zero-shot detection to autonomously generate particle masks across entire images using grid-based prompting. Candidate masks are iteratively produced at grid points, with inherent confidence scoring automatically discarding ambiguous regions.

Manual mode enables targeted particle selection through interactive prompts-positive/negative points, bounding boxes, and rough sketches that SAM refines into accurate masks. This guided promptable segmentation capability is a novel contribution in the field of particle characterization, providing user-controlled analysis. Point prompts allow rapid single-click boundary inference; bounding boxes supply coarse localization tolerant of imprecision; and sketch inputs support iterative refinement for complex cases.

The interactive segmentation system is particularly valuable for selective identification of specific particle populations, analysis of multi-component samples, and focused study of morphological features. This extends the system's utility from automated analysis to expert-guided workflows for specialized research and industrial applications.

The full workflow (Figure 5) includes SAM initialization and preprocessing, user input via point, box, or sketch prompts, real-time predictions with confidence scoring, and iterative refinement supported by history management and mask stack operations.

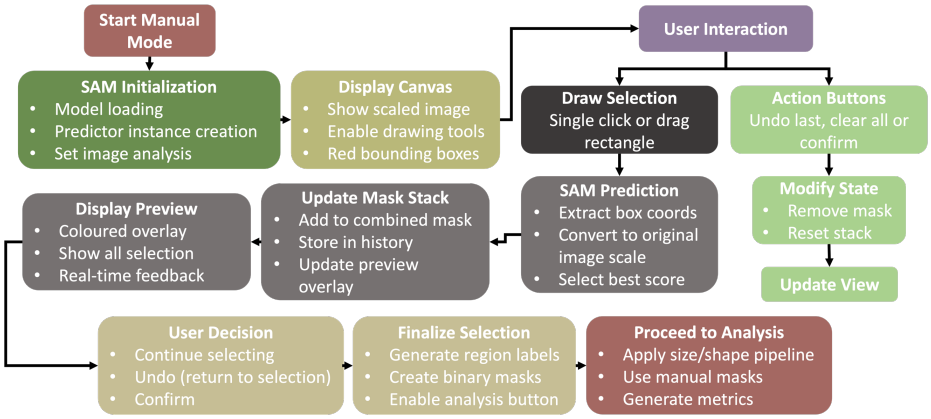

Fig. 5. IPGSS workflow for manual SAM mode. The workflow enables users to iteratively refine image segmentation using bounding boxes and mask operations, with real-time feedback and confidence scoring, before finalizing masks for downstream size/shape analysis.

The IPGSS maintains a history-tracked mask stack with full undo/redo functionality, enabling iterative refinement during exploratory analysis. Each user interaction is precisely mapped from the display scale to the original image coordinates, with transformations accounting for zoom, centering, and pan offsets to ensure spatial accuracy across all interaction modes.

The IPGSS exhibits a high degree of tolerance to imprecise input, consistently generating accurate segmentation masks even when user-drawn bounding boxes are coarse, include background regions, or partially miss particle boundaries. This robustness arises from SAM's boundary-aware feature representations, developed through extensive and diverse pretraining, which enable it to infer true particle extents from minimal localization cues. As illustrated in Figure 6 top panel, even when a bounding box closely borders adjacent particles, the IPGSS precisely segments only the intended target while excluding nearby particles at the boundary, demonstrating its strong capability for spatial discrimination.

The cement particle example in Figure 6 bottom panel further illustrates the flexibility of the manual segmentation mode: under expert guidance, the user can either isolate an entire particle in the tens-of-micrometers range or selectively segment nanoscale

surface features as small as ~30 nm. This capability enables comprehensive multi-scale particle characterization within a unified, interactive workflow.

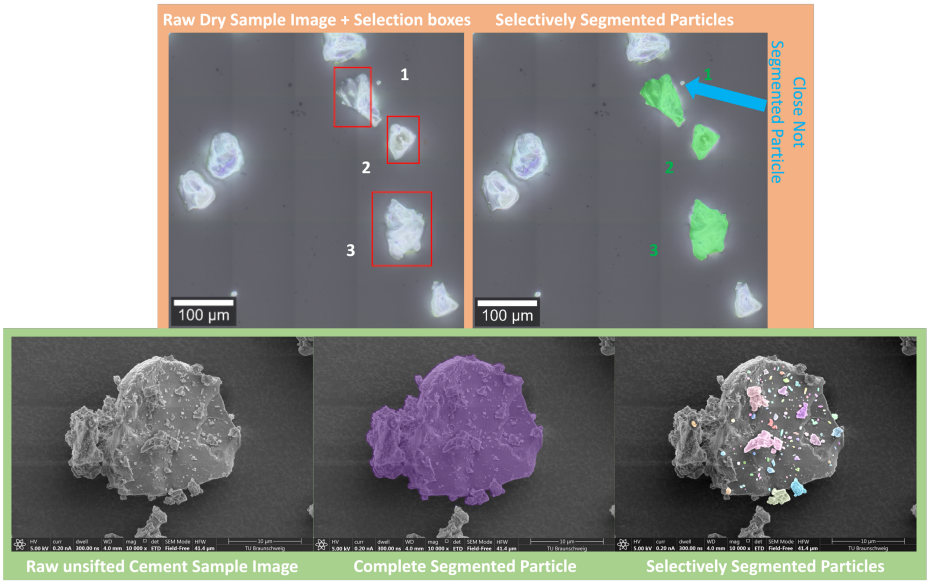

Fig. 6. Manual mode precision in segmentation. (top left) user-provided bounding boxes show coarse localization with background inclusion. (top right) SAM-generated masks accurately isolate target particles, excluding adjacent ones. (bottom) example on cement particles illustrating interactive segmentation, where the user can choose to segment the large particle as a whole or selectively isolate smaller particles on its surface.

Hierarchical Multi-Level Filtering Strategy. The segmentation system's architecture in Figure 7 illustrates the hierarchical particle segmentation and filtering workflow. A complex particle sample image is first encoded into image embeddings and processed through SAM's lightweight mask decoder, guided by a prompt encoder that accepts positional (x, y) coordinates together with foreground (fg) and background (bg) point prompts, or alternatively, bounding box coordinates (x_1, y_1) and (x_2, y_2). SAM's internal confidence scoring initially filters out low-quality masks, after which configurable microscopy-specific filters based on area, gradient magnitude, and circularity further refine the candidate regions. This integration ensures robust and reliable particle identification across diverse imaging conditions while maintaining analytical precision.

The architecture uses a four-stage filtering workflow, starting with SAM's confidence scores and extending with custom microscopy-oriented filters introduced in this work. This layered approach ensures robust particle identification across diverse particle systems and imaging conditions while prioritizing analytical precision over detection completeness. The first stage leverages SAM's transformer-based confidence scoring, which includes stability scores, quality prediction algorithms, and attention-based

uncertainty estimation. Candidate masks with low confidence are automatically discarded through configurable thresholds, removing ambiguous boundaries and poorly defined objects at the source. The second stage applies area-based statistical filtering to enforce expected size ranges, removing very small objects that likely represent noise or debris and rejecting oversized agglomerates that may correspond to clusters or imaging artifacts. A configurable minimum area threshold is applied, with a default range of 10–1000 pixels, though this can be adjusted depending on particle size and image resolution.

The third stage applies element-based threshold filtering to enhance particle background separation. A configurable intensity threshold is used to exclude regions with poor contrast or weak signal definition. The final stage imposes circularity-based morphological filtering with user-configurable thresholds (default minimum circularity of 0.8) to eliminate highly irregular objects, which often arise from segmentation artifacts, agglomerate fragments, or non-particle structures. This step retains both spherical and irregular but valid particles, ensuring flexibility while removing obvious false positives.

Together, these four filtering layers form a conservative architecture that enhances the reliability of particle segmentation for quantitative characterization. Independent threshold adjustment at each stage allows the SS to be adapted to different imaging conditions and particle systems.

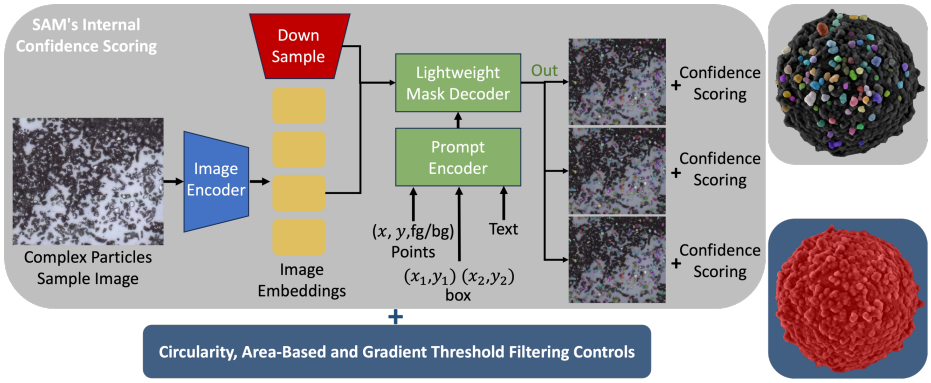

Fig. 7. Hierarchical filtering architecture for particle segmentation. SAM processes input images using positional (x, y) and foreground (fg)/background (bg) prompts. Candidate masks are screened by confidence scoring and refined by area, gradient, and circularity filters for robust particle identification across imaging conditions. (right) two examples on the showing a common issue in complex microscopy images: SAM may misinterpret object boundaries and split a single particle into multiple masks. The added circularity-, area-, and gradient-based filters correct these errors by guiding the system toward true particle regions and preventing such mis-segmentation.

Evaluation Against Conventional Methods. To demonstrate the advantages of the transformer-based approach, comparative analysis was performed on >20 complex aluminum oxide images using three segmentation strategies: the SAM-based segmentation system, OpenCV edge-based segmentation, and Cellpose deep learning segmentation.

OpenCV represented traditional computer vision, combining gradient-based edge detection with contour extraction to delineate particle boundaries. Cellpose represented the state-of-the-art in microscopy segmentation, using a flow-based deep learning model trained on microscopy images to predict gradient fields toward particle centers, enabling segmentation of touching or overlapping objects.

The evaluation focused on challenging dispersed samples with high particle density and overlap, representative of practical characterization scenarios in materials processing and quality control. Performance was assessed through both qualitative visual inspection and quantitative comparison of particle counts and size distributions against QICPIC reference measurements.

2.3 Zero-Shot Depth-Aware Surface Roughness Analysis

DPT Architecture and Implementation. The depth estimation component uses DPT-Large with a ViT-L/16 backbone, trained within the MiDaS framework on a diverse mixture of datasets including NYU Depth V2 and KITTI. This heterogeneous training enables the model to learn strong monocular depth cues such as shading gradients, texture variation, and global geometric structure that transfer effectively to microscopy despite the substantial domain shift. The approach introduces a novel depth-based methodology for particle roughness analysis, reconstructing the full SEM-visible surface region of each particle from a single image. This offers markedly broader surface coverage than AFM, which typically samples less than 5% of the particle's area, while avoiding the specialized instrumentation, intricate preparation steps, and calibration procedures required for AFM measurements. The zero-shot capability further enhances accessibility by eliminating the need for domain-specific training data.

DPT implements hierarchical feature extraction, processing images at multiple resolutions and fusing them through a feature pyramid network. This enables depth maps at full resolution that preserve fine-scale textures while maintaining global geometric consistency. Zero-shot performance arises from pretraining across diverse depth estimation scenarios, learning cues from shading gradients, textures, specular highlights, and perspective effects. These priors transfer directly to SEM images, where electron scattering encodes surface topography. The full depth-aware roughness workflow (Figure 8) begins with SEM input, followed by zero-shot DPT depth estimation with multi-scale processing. Depth maps are converted into 3D point clouds with real-world scaling, filtered to remove substrates, and analyzed with ISO-standard roughness metrics, producing five complementary measures of surface texture through electron scattering and secondary electron emission patterns.

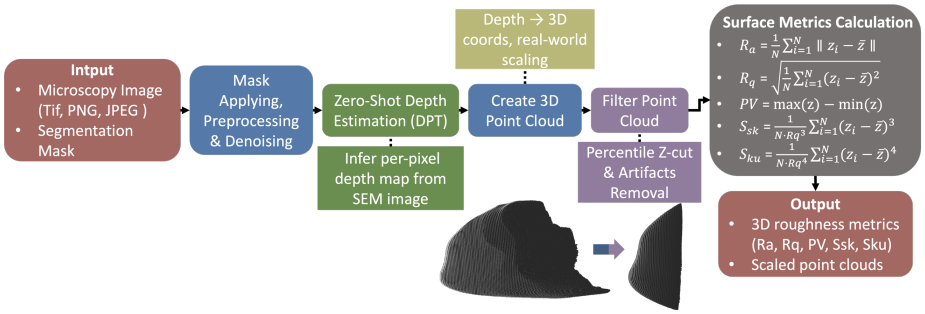

Fig. 8. DRCS's architecture: SEM images with segmentation masks are processed using DPT to generate scaled 3D point clouds. Percentile-based filtering removes substrate artifacts, and ISO-standard roughness parameters (R_a, R_q, PV, S_{sk}, S_{ku}) are computed as quantitative surface descriptors.

3D Point Cloud Generation and Real-World Scaling Protocols. Depth-to-3D conversion uses inverse perspective projection with real-world scaling based on particle dimensions from image metadata or user input. Pixel coordinates and relative depths are transformed into 3D Cartesian coordinates with nanometer units. Table 1 summarizes the coordinate transformation and scaling parameters.

Table 1. 3D Point Cloud Generation and Scaling Parameters

Parameter	Description	Typical Value
xy_scale	Lateral spatial resolution (nm/pixel)	1.836 nm/pixel
z_scale	Depth scaling factor (nm/depth unit)	Derived from hemispherical assumption
Physical width	Particle diameter from image metadata	~2000 nm (2 µm)
Image width	Image resolution	2048 pixels
Expected height	Half of particle diameter for spheres	Physical width / 2
Percentile threshold	Z-value cutoff for substrate removal	40th percentile

The lateral resolution (xy_scale) is obtained by dividing the physical particle width derived from SEM metadata or scale calibration by the image width in pixels, yielding the nanometer-per-pixel factor used to scale the x–y coordinates of the reconstructed point cloud. The depth scaling factor (z_scale) converts the model's relative depth units into physical height by assuming that each particle approximates a hemisphere, where the expected height equals half of the measured particle diameter. This links the predicted depth range to the actual particle geometry, ensuring that reconstructed height values are physically meaningful. The physical width parameter represents the particle's real-world diameter, while the image width corresponds to the SEM resolution (e.g., 2048 px) defining the sampling density across the field of view. The expected height, calculated as physical width divided by two, provides the geometric reference

needed to align the depth map with the hemispherical assumption. Point cloud refinement employs percentile-based Z-thresholding to separate the particle surface from the substrate. A cutoff near the 40th percentile is typically applied, removing low-lying depth values associated with the background and the particle-substrate interface. This preserves the upper ~60% of the particle surface, where depth estimates are most reliable and contain the topographical features essential for roughness quantification.

ISO-Standard Surface Roughness Analysis. Surface roughness evaluation follows ISO 4287/4288 standards, applying five complementary metrics to the filtered three-dimensional point cloud obtained after substrate removal. Let N denote the total number of surface points in the point cloud, z_i the height of point i (in nanometers), and $\bar{z} = \frac{1}{N}\sum_{i=1}^{N} z_i$ the mean surface height. The corresponding parameters are summarized in Table 2. The arithmetical mean deviation R_a quantifies the average absolute deviation of surface heights from the mean plane and represents the most widely reported roughness descriptor. The root-mean-square roughness R_q is more sensitive to large deviations and typically exceeds R_a by 10–25%. The peak-to-valley height PV expresses the maximum height difference across the surface, capturing extreme topographical features. Skewness S_{sk} characterizes asymmetry in the height distribution, with negative values indicating valley-dominated surfaces and positive values indicating peak-dominated surfaces. Kurtosis S_{ku} describes the tailedness of the distribution; values greater than 3 correspond to spiky surfaces with pronounced peaks, whereas values below 3 indicate flatter topographies.

Table 2. ISO-Standard Surface Roughness Parameters

Parameter	Formula	Description
R_a	$\frac{1}{N}\sum_{i=1}^{N} \parallel z_i - \bar{z} \parallel$	Arithmetical mean deviation - average absolute deviation from mean height
R_q	$\sqrt{\frac{1}{N}\sum_{i=1}^{N}(z_i - \bar{z})^2}$	Root mean square roughness - enhanced sensitivity to large variations
PV	$\max(\mathrm{z}) - \min(\mathrm{z})$	Peak-to-valley height - maximum height difference
S_{sk}	$\frac{1}{N \cdot Rq^3}\sum_{i=1}^{N}(z_i - \bar{z})^3$	Skewness - asymmetry of height distribution
S_{ku}	$\frac{1}{N \cdot Rq^4}\sum_{i=1}^{N}(z_i - \bar{z})^4$	Kurtosis - tailedness of height distribution

Advanced Morphological Parameter Analysis. The morphological analysis system implements seven shape parameters according to ISO 9276-6 and ISO 13322-2, ensuring compatibility with commercial QICPIC dynamic image analysis systems. Calculations use exact geometric algorithms rather than approximations to maximize accuracy and minimize systematic errors (Table 3). Here, A denotes particle area, P perimeter, F_{min} and F_{max} the minimum and maximum Feret diameters, P_{convex} the convex hull perimeter, and P_{circle} the perimeter of a circle with equivalent area.

Table 3. Morphological Shape Parameters

Parameter	Formula	Description
Aspect Ratio	$\frac{F_{min}}{F_{max}}$	Ratio of minimum to maximum Feret diameter (Range: 0-1)
Sphericity	$\frac{\sqrt{4\pi A}}{P}$	Circle-equivalent perimeter ratio (Range: 0-1)
Convexity	$\frac{P_{convex}}{P}$	Ratio of convex hull to actual perimeter (Range: 0-1)
Elongation	$1 - \frac{F_{min}}{F_{max}}$	Alternative aspect ratio representation (Range: 0-1)
Roundness	$\frac{4A}{\pi F_{max}^2}$	Circle-equivalent area ratio (Range: 0-1)
Circularity	$\frac{4\pi A}{P^2}$	Isoperimetric quotient (Range: 0-1)
Perimeter Regularity	$\frac{P_{circle}}{P}$	Boundary smoothness indicator (Range: 0-1)

Feret diameters are computed using the rotating calipers method, which provides true geometric accuracy by evaluating all orientations. The minimum Feret diameter (breadth) represents the narrowest projected width, the maximum (length) the widest, and their ratio defines the aspect ratio. Statistical analysis follows Q3-based percentile calculations (DIN 66141), computing the 10th percentile (D_{10}, fine particles), median (D_{50}, representative particles), and 90th percentile (D_{90}, coarse particles), with the median mainly used for comparative analysis.

2.4 Validation Methodology

Dual Validation Framework. The validation strategy applies domain-specific protocols to comprehensively assess the pipeline's performance across size, shape, and surface roughness. Size and shape validation employed aluminum oxide samples imaged with a WITec alpha300 R optical microscope under controlled conditions, with systematic comparison against QICPIC reference measurements from ~950,000 particles per

condition. Surface roughness validation used the Hülagü et al. dataset, which provides ground truth from AFM and profile-based methods.

Statistical Validation Protocols. The validation protocols assess both accuracy (agreement with reference values) and precision (repeatability). For size and shape, percentile comparisons and morphological parameter distributions are directly evaluated against QICPIC standards to quantify systematic bias and variability. Individual image analyses with 50–500 particles provide sufficient sampling for morphological distribution characterization, while combined multi-image datasets of 1000–3000 particles enable robust percentile calculations comparable to industrial reference standards. For comparative segmentation evaluation, analyzing >20 complex images per method ensures consistent performance assessment across diverse sample conditions. For surface roughness, Bland-Altman analysis evaluates inter-method agreement by calculating mean differences (systematic bias). Correlation analysis using Pearson coefficients measures the strength of linear relationships between methods, verifying whether relative roughness rankings are preserved despite systematic scaling differences.

3 Results and Discussion

3.1 Segmentation Performance Evaluation

Segmentation Results on Aluminum Oxide Samples. The SAM-based segmentation system successfully segmented aluminum oxide particles under both dispersed and dry preparation conditions, producing high-quality binary masks and particle identifications suitable for quantitative morphological analysis. Representative results (Figure 9) show accurate boundary delineation across preparation protocols.

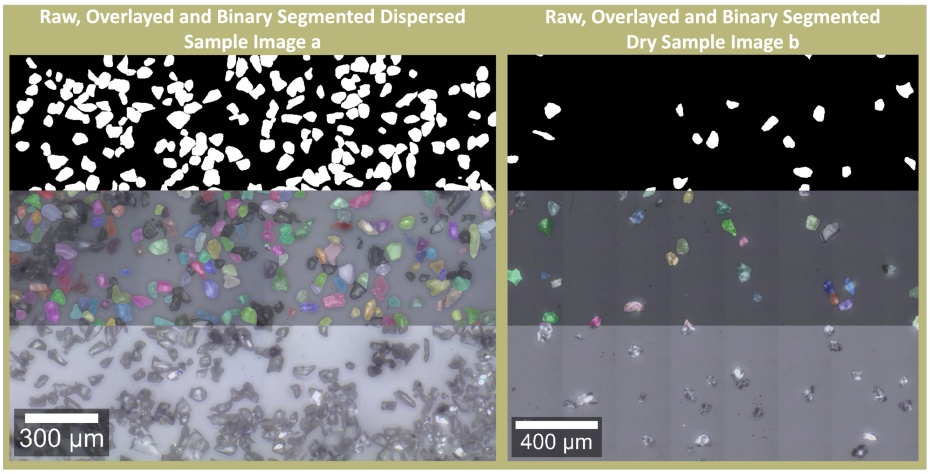

Fig. 9. Particle segmentation results for optical microscopy images of aluminum oxide powders. Left column: dispersed sample (image a) and Right column: dry sample (image b). For each condition, top row shows binary segmentation masks, middle row displays color-coded particle labels, and bottom row presents raw images.

The dispersed sample image a (Figure 9, left) contained well-separated particles, enabling robust automated segmentation of 528 particles from a single image. The binary mask demonstrates clean boundary definition, while color-coded labeling confirms correct separation of individual particles. The dry sample image b (Figure 9, right) yielded 75 detected particles. These segmentation outputs form the basis for subsequent morphological analysis, where boundary quality directly determines measurement accuracy. The hierarchical filtering strategy ensures that only high-confidence particles passing all quality criteria are included in quantitative evaluations.

Multi-Level Filtering Strategy Performance. The hierarchical filtering cascade effectively maintained measurement precision in complex particle fields by distinguishing valid particles from artifacts such as noise, agglomerates, and poorly defined objects. By combining SAM's confidence scoring with microscopy-specific filters, the segmentation system prioritized analytical precision over detection completeness, ensuring robust identification for quantitative analysis (Figure 10, right). This conservative strategy is particularly important in automated workflows, where false positives could compromise process decisions.

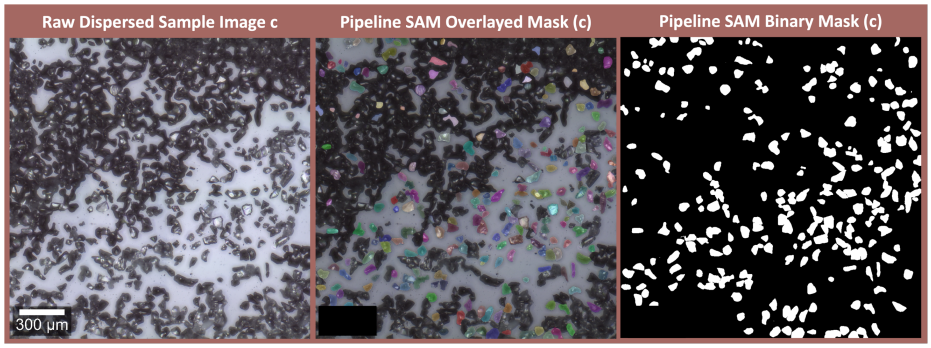

Fig. 10. Multi-level filtering strategy applied to agglomerated sample (image c). Left: raw micrograph with overlapping particles. Middle: SAM segmentation with colored overlays of particles retained after filtering. Right: SAM segmentation binary mask

The approach markedly reduced detected objects while preserving visually accurate particle identification. Problematic regions including partially occluded particles, edge artifacts, and ambiguous boundaries were successfully eliminated (Figure 10, middle). The integration of confidence thresholding, area-based statistical filtering, gradient magnitude assessment, and circularity evaluation provides a level of quality control not achievable with SAM's inherent single-stage filtering.

Comparative Analysis: Segmentation System vs. Conventional Methods. Comparative evaluation across >20 complex dispersed aluminum oxide images revealed fundamental differences between the transformer-based SAM Segmentation System, OpenCV (traditional edge-based vision), and Cellpose (state-of-the-art deep learning trained for microscopy).

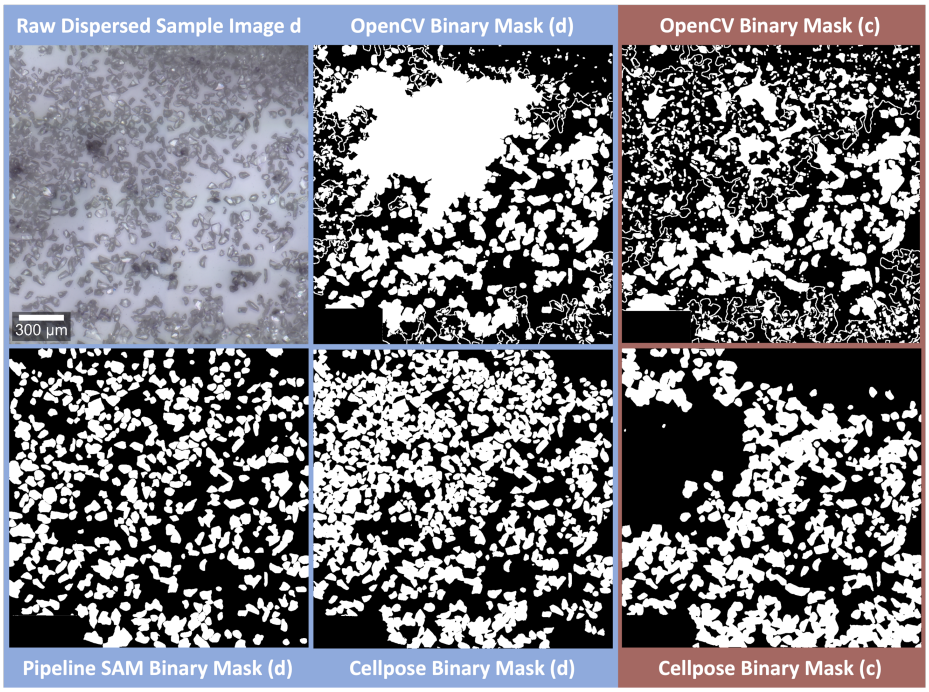

Fig. 11. Segmentation comparison on a dispersed aluminum oxide sample. Top row: raw image (d) and OpenCV masks, showing fragmented and inconsistent results. Bottom row: segmentation system and Cellpose masks for images d and c (raw and segmentation system masks of c shown in Figure 10), both yielding more coherent particle segmentations than OpenCV.

In the first dispersed sample (Figure 3d, blue background), OpenCV produced fragmented boundaries, while the segmentation system preserved particle individuality and closely matched QICPIC references. Cellpose generated coherent masks but frequently merged adjacent particles, inflating size estimates by 25–100% relative to QICPIC, with errors increasing for closely spaced particles. A similar trend appeared in the second sample (Figure 3c, orange background), where OpenCV again failed and Cellpose performed better but remained imperfect. In contrast, the segmentation system achieved particle counts and size distributions closely matching QICPIC, outperforming both baselines through transformer-based boundary reasoning and hierarchical multi-stage filtering that enabled accurate, training-free segmentation across diverse microscopy conditions.

3.2 Size and Shape Validation Results

QICPIC Reference Measurements and Statistical Foundation. The QICPIC dynamic image analysis system provided statistically robust reference measurements based on approximately 950,000 particles per condition, establishing a solid foundation for validation. Under dispersed conditions, particle sizes ranged roughly from 20 µm to 80µm with D_{50} of about 50µm, closely matching the manufacturer's specified value and confirming the accuracy of the reference measurements. Under dry conditions, a shift toward larger apparent sizes was observed, consistent with particle agglomeration effects.

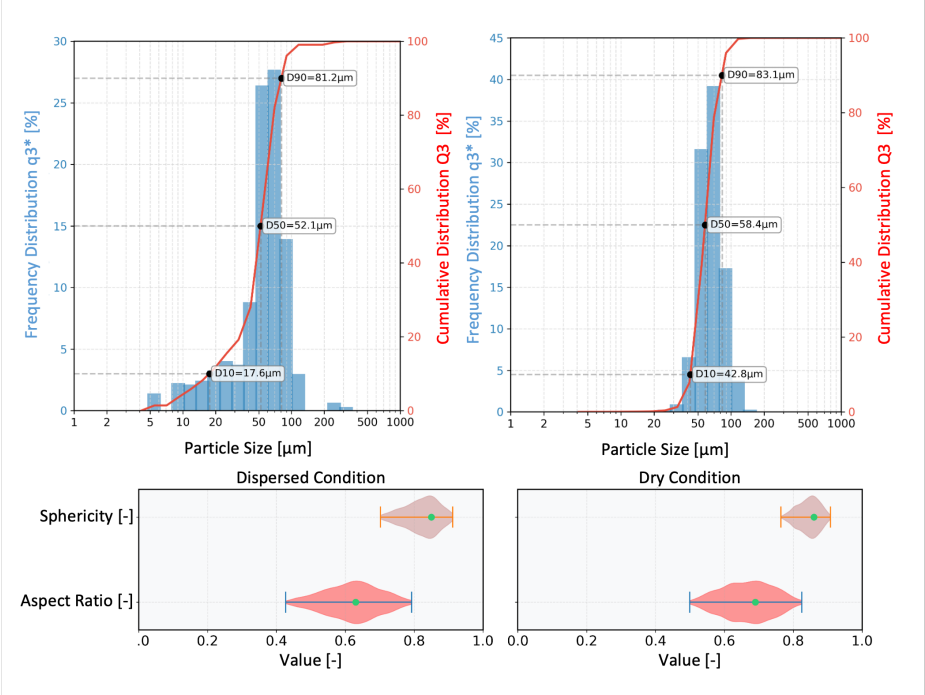

Fig. 12. QICPIC reference measurements establishing ground truth distributions. Top panels: PSD under dispersed (left) and dry (right) conditions showing both frequency and cumulative distributions. Bottom panels: morphological parameter distributions for sphericity and aspect ratio demonstrating measurement precision and statistical robustness from ~950,000 particles per condition.

Dry conditions exhibited a pronounced shift toward larger particle sizes, corresponding to a 143% increase in D_{10} (fine fraction), a 12.1% increase in D_{50} and a 2.1% increase in D_{90} (coarse fraction) (Figure 12, top panels). This reflects differential effects of sample preparation across the size distribution. The trend likely arises from partial dissolution of aluminum oxide particles under aqueous dispersed conditions, where surface interactions with water slightly reduce particle size relative to the pristine dry state. The pronounced increase in D_{10} indicates that small particles are most affected, consistent with enhanced dissolution at high surface-area-to-volume ratios.

Morphological parameter distributions from QICPIC measurements (Figure 12, bottom panels) highlight clear, but modest, preparation effects. Under dispersed conditions, aspect ratio concentrates around 0.60–0.70 (whiskers ~0.45–0.80), indicating well-separated particles with limited orientation bias, while sphericity clusters near 0.85–0.90 (whiskers ~0.82–0.92), consistent with near-spherical morphology. Under dry conditions, aspect ratio shifts slightly higher to ≈0.65–0.75 (whiskers ~0.55–0.85), and sphericity shows a slightly broader distribution ≈0.82–0.90 with a similar center, consistent with mild orientation and occasional agglomeration introduced during dry preparation.

Performance Across Dispersed Conditions. Validation on dispersed samples demonstrated consistent measurements across imaging sessions and sample sizes. Single-image analysis yielded a D_{50} of 60.9µm with a size range of approximately 45–75µm, while combined analysis of 10 images (2,998 particles) resulted in D_{50} = 56.4µm with a range of about 40–70µm (bottom Figure 13). The multi-image analysis confirms the improved statistical representativeness achieved through larger sample sets.

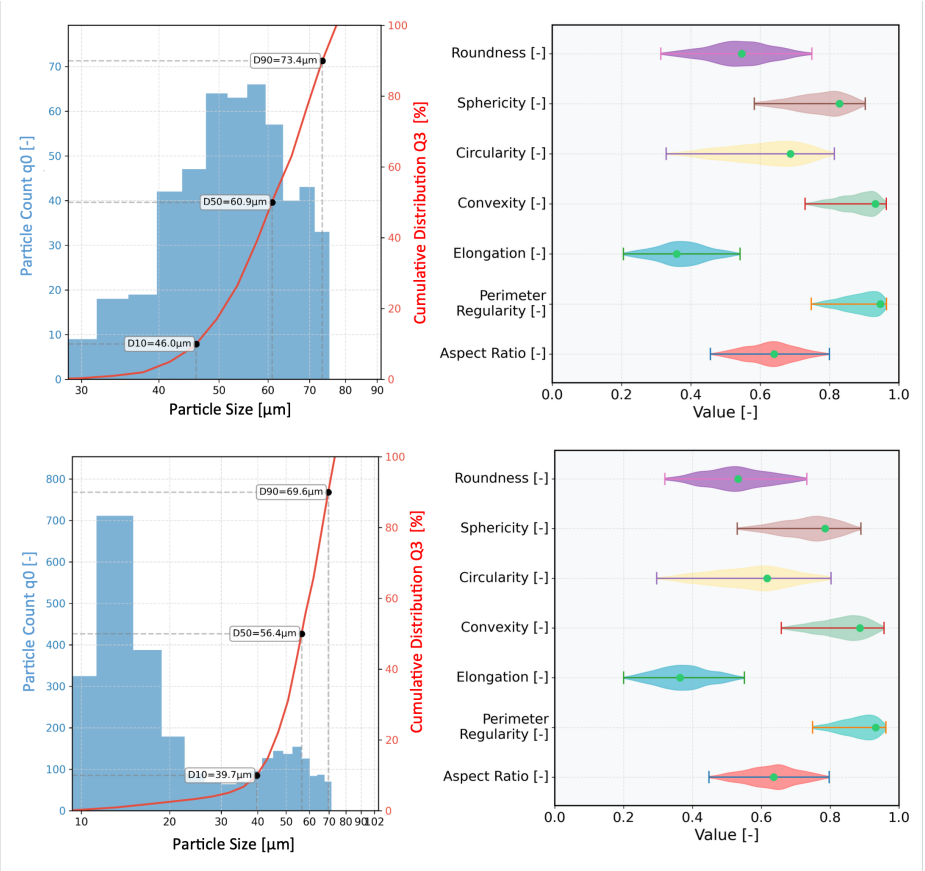

Fig. 13. Segmentation system's PSD analysis for dispersed aluminum oxide samples. Top panel: single-image analysis of image a (Figure 9) with corresponding morphological parameter distributions. Bottom panel: combined analysis of 10 images with 2,998 detected particles, demonstrating improved statistical representation with larger sample sizes.

Relative to QICPIC reference data, the segmentation system produced slightly higher fine-fraction values (D_{10} = 39–46µm vs. 17.6µm), primarily due to optical resolution limits and conservative filtering that exclude particles smaller than ~10–15 pixels. D_{50} showed close agreement with the reference value of 52.1 µm, deviating by only 5.5–17%, confirming reliable accuracy in the core size range. These differences reflect expected methodological contrasts rather than segmentation errors.

Morphological metrics (Figure 13, right) further validated segmentation quality. Roundness values clustered around 0.8–0.9, indicating well-separated particles with minimal agglomeration, while sphericity (0.7–0.8) and aspect ratio (0.6–0.8) distributions were consistent with near-spherical aluminum oxide morphology. Convexity (0.95–1.0) and perimeter regularity (0.9–1.0) remained high, confirming smooth particle boundaries and minimal segmentation artifacts.

Dry Sample Analysis and Preparation Effects. Analysis of dry samples revealed distinct size characteristics compared to dispersed conditions. Single-image analysis yielded a D_{50} of 61.6µm with a size range of approximately 45–75µm, while combined analysis of 11 images (941 particles) produced D_{50} = 62.8µm with a range of about 45–80µm (Figure 14). The close agreement between single- and multi-image results confirms excellent measurement consistency under dry conditions.

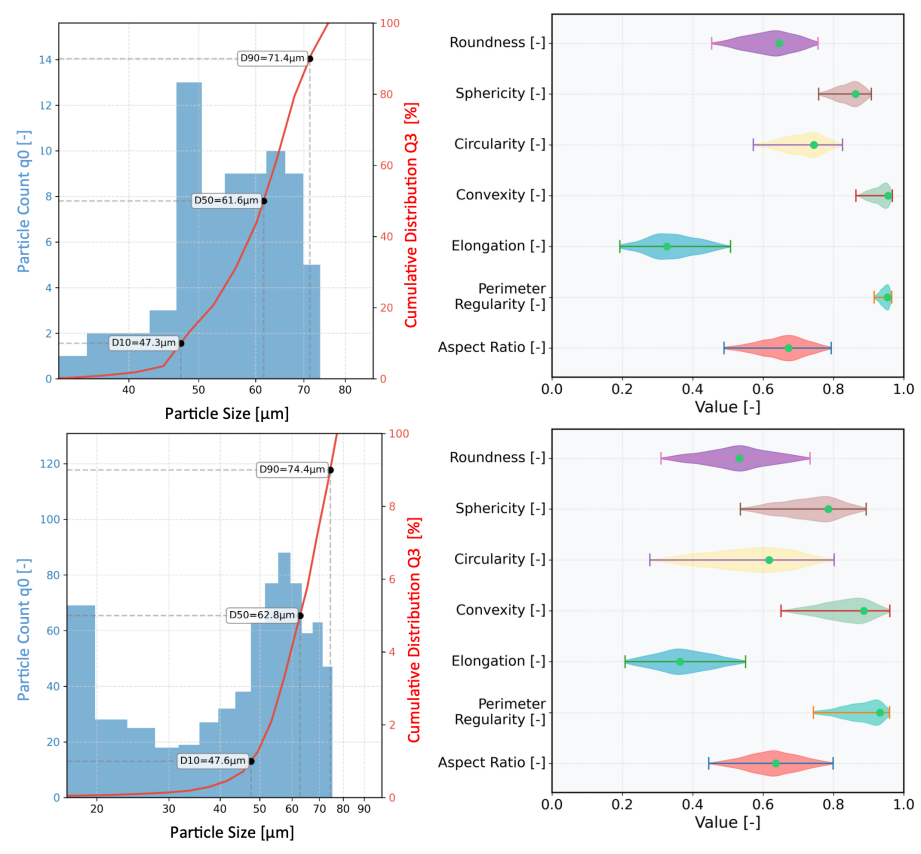

Fig. 14. Segmentation system's analysis results for dry aluminum oxide samples. Top panel: single-image analysis of image b (Figure 9) with corresponding morphological parameter distributions. Bottom panel: combined analysis of 11 images with 941 detected particles, showing improved statistical representation and revealing increased variability in morphological parameters due to particle orientation effects in dry preparation.

Compared to dispersed samples, dry samples exhibited higher D_{10} values (47.3–47.6µm vs. 39.7–46.0µm), supporting the interpretation that aqueous dispersion causes slight particle dissolution rather than agglomeration in dry conditions. D_{50} values showed modest increases, while D_{90} remained similar.

Morphological parameter distributions (Figure 14, right) displayed greater variability under dry preparation. Aspect ratios broadened (0.4–0.8) due to orientation effects on the substrate, whereas dispersed particles in suspension showed narrower ranges. Sphericity values extended from 0.6–0.9 versus 0.7–0.8 in dispersed samples. Convexity dropped to 0.85–0.95 compared to 0.95–1.0, reflecting more irregular boundaries. Perimeter regularity decreased to 0.8–0.9 versus 0.9–1.0, consistent with substrate interactions and edge effects.

3.3 Surface Roughness Validation Analysis

Fundamental Differences in Measurement Methodologies. Surface roughness validation highlights fundamental differences between methods that extend beyond simple scaling. The profile method derives roughness from 2D particle boundary fluctuations, capturing edge irregularities caused by surface features intersecting the silhouette. While effective for contour-level variations, it cannot probe surface topology away from the boundary. AFM provides direct 3D topography but is limited to localized regions of the surface. Although highly resolved, such measurements may not represent overall roughness for particles with heterogeneous features or synthesis-induced surface variations.

The depth-based approach introduced here analyzes the entire visible hemisphere (~50% of surface area) from a single SEM image, providing intermediate-scale coverage between AFM's localized measurements and global boundary methods. This broader sampling yields more representative assessments of particle surface characteristics, while also democratizing roughness analysis by removing the need for specialized expertise and AFM instrumentation.

Single-Particle Reconstruction and Multi-Perspective Visualization. Representative reconstruction of particle 5 demonstrates the depth-based method's ability to generate high-quality 3D surfaces from standard SEM images (Figure 15). The SEM image (Figure 15 left) shows complex textures typical of the analyzed particles. The depth map (Figure 15 middle) captures a realistic hemispherical profile with clear surface variations, reflecting the zero-shot capability of transformer-based depth estimation. The quantitative depth scale visualization (Figure 15 right) spans 1532–1880 nm, confirming accurate recovery of surface relief and fine-scale texture.

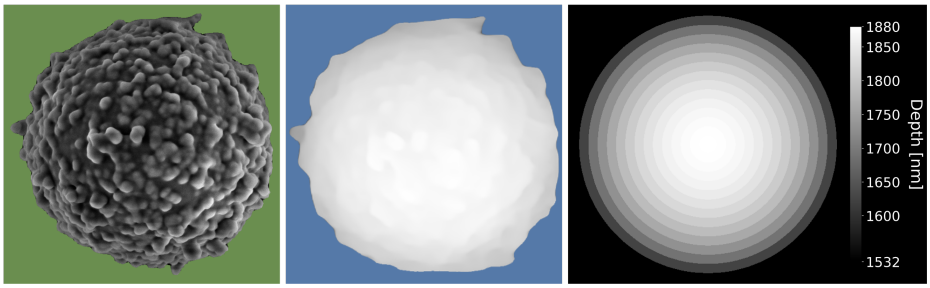

Fig. 15. Left: input particle 5 SEM image showing detailed surface morphology. Middle: DPT-generated depth map with realistic hemispherical profile. Right: quantitative depth scale (1532-1880 nm range) enabling precise surface roughness quantification with 348nm total relief.

The complete workflow (Figure 16) illustrates the transformation from original SEM image of particle 9 (top middle) through segmentation (bottom left) and depth estima-

tion (bottom middle) to 3D reconstruction (bottom right). The depth map shows realistic surface features, while the point cloud (right) reconstructs the full visible hemisphere.

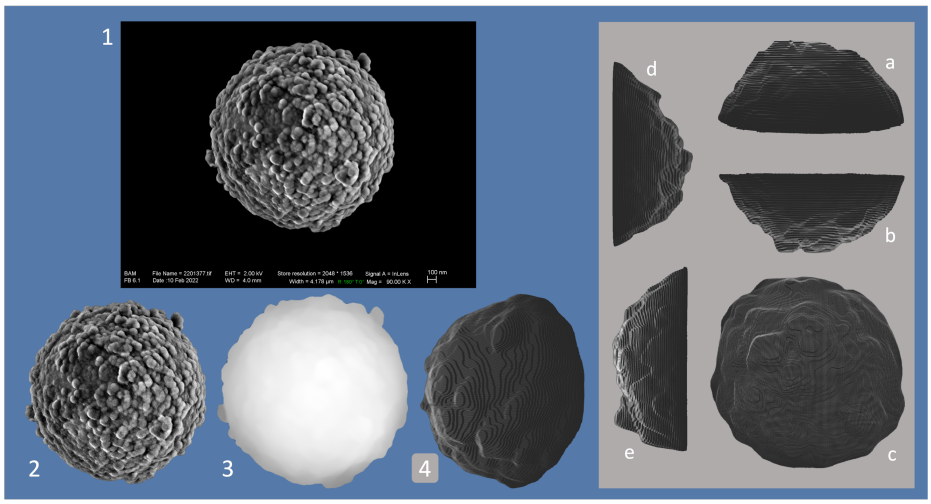

Fig. 16. Complete 3D reconstruction and visualization system for particle 9. left: (1) Original SEM image, (2) segmented particle, (3) inferred depth map, and (4) 3D reconstructed surface view. Right Panels (a–e): show different point cloud perspectives of the reconstructed particle: (a) bottom view, (b) top view, (c) front view, (d) left side view, and (e) right side view.

Multi-perspective views (Figure 16, right) reveal information inaccessible from single-view SEM images. The visualization suite provides top views of surface texture distribution, bottom views of substrate interfaces, textured renderings highlighting fine-scale details, side profiles of hemispherical geometry, and cross-sections exposing internal surface profiles and roughness length scales. This capability enables detection of anisotropy, curvature variations, and spatial roughness distributions offering morphological insights into synthesis effects beyond traditional 2D analysis.

Depth-Based Reconstruction Performance Across All Particles. The depth-based system successfully analyzed surface roughness across all nine core-shell microparticle samples, demonstrating clear differentiation between particle types and synthesis batches. The complete processing workflow from original SEM images through 3D reconstruction to final surface analysis is shown in Figure 17.

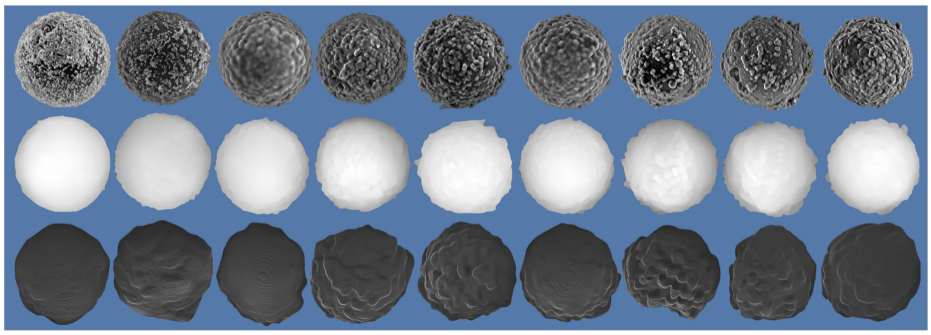

Fig. 17. Overview of particle analysis results for all nine analyzed particles. Top row: original segmented SEM images showing surface morphology variations. Middle row: DPT processed depth maps. Bottom row: 3D reconstructed surfaces revealing hemispherical profiles and texture details.

The overview in Figure 17 demonstrates the DRCS's ability to analyze particles with systematically varied architectures. Successful reconstruction across all samples validates the hemispherical assumption used in depth-to-point-cloud conversion, where particle height is set to half the diameter. Particles 1 exhibits smoother surfaces in both the SEM images and the 3D reconstructions, with depth maps showing relatively uniform height variations consistent with single-shell synthesis. In contrast, Particles 3 through 9 represent core–shell–shell structures and display progressively more complex surface textures, with reconstructed 3D models and depth maps revealing heterogeneous roughness across multiple length scales. Batch-to-batch differences are apparent in the reconstructions, and the systematic progression from smoother to increasingly complex particles highlights the DRCS's sensitivity to surface architecture induced by synthesis conditions.

Validation Against Profile Method Benchmarks. For the nine selected validation particles, only profile-method roughness values were consistently available from Hülagü et al.. Although AFM measurements were reported in the same study, they were not performed on all particles and therefore could not be used for direct, paired comparison in our validation set. However, because AFM was used to verify the accuracy of the profile method in that work, the profile measurements constitute an appropriate and experimentally validated baseline for the present evaluation.

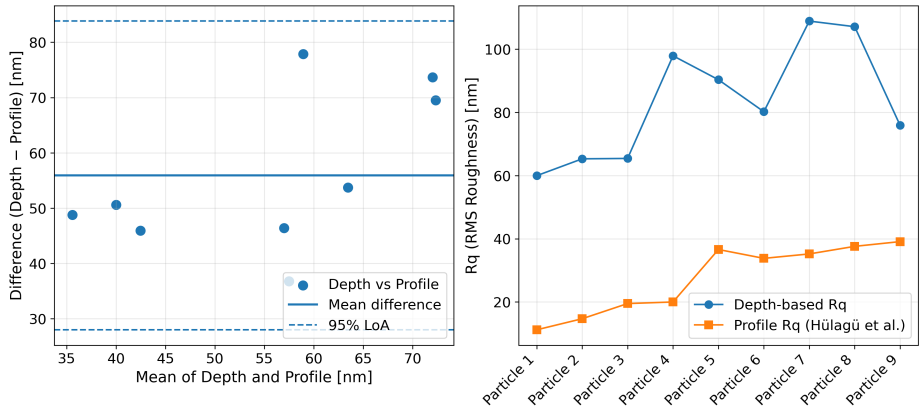

Fig. 18. Validation of depth-derived roughness against the contour-based profile method for Particles 1–9. Left: Bland-Altman plot showing a consistent positive offset and 95% limits of agreement, indicating systematic rather than random deviation. Right: Comparison of depth-based and profile-derived Rq values across the particle set, illustrating preservation of relative roughness trends despite differences in absolute scale.

A systematic comparison between the depth-based roughness estimates and the profile-derived Rq values revealed a consistent positive bias. Bland–Altman analysis (Figure 18, left) indicated an average difference of +55.9 nm, with 95% limits of agreement of ±27.9 nm. The offset between the two methods is therefore stable, reproducible, and quantifiable, suggesting that it originates from methodological differences rather than stochastic variation. The profile method captures roughness along a single contour, whereas the depth-based approach incorporates surface variability across a larger hemispherical region, and the observed amplification appears to reflect this fundamental difference in sampling rather than an intrinsic failure of the method. Even so, the magnitude of the divergence highlights the need for calibration if absolute numerical comparability is required.

Despite these scale discrepancies, the depth-based method preserved the relative ordering of particle roughness (Figure 18, right). Across Particles 1–9, it reproduced the same monotonic trend obtained from the profile method and correctly distinguished smoother from rougher surfaces. Correlation analysis yielded $r \approx 0.64$, meaning that roughly 40% of the variance in classical contour-based roughness is captured by the depth approach. Although this does not represent perfect agreement, it demonstrates that the method retains meaningful information about surface complexity and is not dominated by random noise or artefacts.

Depth-derived roughness values were on average approximately 3.4 times higher than the corresponding profile values, with ratios ranging from 1.9 to 5.4 across Particles 1–9. Profile Rq for the validation set spanned 11.2–39.1nm, while depth-based values ranged from 59.9–108.9nm. This systematic scaling is consistent with the ex-

pected behavior of a method that samples a larger portion of the three-dimensional surface. Although such amplification complicates direct numerical matching, the consistent and predictable offset provides a clear pathway for calibration. Once calibrated, the depth-based approach may offer a more representative measurement of fine-scale texture, especially in contexts where full-surface morphology rather than boundary contours is physically relevant.

3.4 SSB Application Case Study

For battery process engineering, the proposed IPGSS provides a useful capability to characterize (sub)-micron-sized particles, which are particularly relevant during SSB development. In this field, SSB composite cathodes demand tailored PSD for the active material and the solid electrolyte (SE) to enable a functional microstructure. Thereby, the PSD of the SE often needs to be adapted via comminution and requires corresponding quality control. Conventional laser-diffraction methods face challenges in this context (Figure 19) as agglomerates are easily measured instead of primary particles, thus overestimating true particle morphology of the SE [56,57,58]. Moreover, identifying a truly inert solvent for wet analysis of SEs is challenging but necessary, since any reaction with the electrolyte could alter its morphology and shift its apparent PSD [59,60]. Also, dry laser diffraction is not straightforward for SEs, since these materials are often air- and moisture sensitive. Lastly, the morphology of the particles is neglected in conventional laser diffraction methods, but in the field of SSB, morphology can have a significant impact on the microstructure of the electrode and thus the electrochemical performance [61,62].

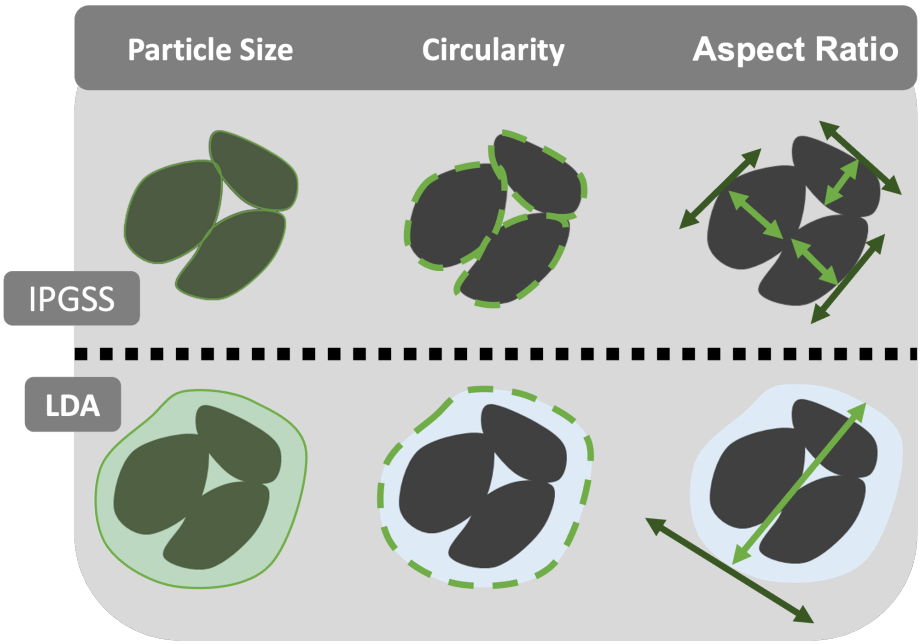

Fig. 19. Comparison of IPGSS's and laser-diffraction analyzer's (LDA) analysis approaches for agglomerated SE powders. The IPGSS captures true primary particle size and morphology, while LDA reflects agglomerate-level features.

The capability of IPGSS to resolve primary particles within strongly agglomerated SEs is demonstrated here using the example of Li_3InCl_6 (LIC). This electrolyte was synthesized via a solvent-based route [63] and subsequently comminuted for 8 min at 600 rpm. As shown in Figure 20 top left panel, the comminuted powder contains both small primary particles as well as larger agglomerated LIC clusters. A magnified view of one agglomerate (Figure 20 top right panel) reveals that these clusters are predominantly composed of submicron-sized primary particles. However, typical wet laser diffraction measurements primarily detect these agglomerated clusters, resulting in a broad PSD, with a median particle size of $x_{50} = 9.47\mu m$ (Figure 20 bottom left panel). This highlights a fundamental limitation of conventional measurement techniques for SEs as accurate particle size determination is often compromised by agglomeration effects and solvent interactions. Since the SEs particle size plays a critical role in determining the microstructure of the composite electrode and has a pronounced impact on overall cell performance, precise characterization methods such as the proposed pipeline are essential for advancing SSB technology.

Using guided image analysis, it is possible to accurately identify and quantify the primary particles contained within SE agglomerates. To illustrate the impact of this capability, the IPGSS was applied to analyze the primary particles within a single LIC agglomerate (Figure 20 bottom right panel). The resulting particle size distribution differs markedly from that obtained by conventional laser diffraction, revealing the presence of significantly smaller particles, with a median size of $x_{50} = 0.54\mu m$. However, it should be noted that SEM-based image analysis typically involves a much smaller number of particles (in this case, ~150), which increases the likelihood of statistical errors. Therefore, for reliable quantitative evaluation, a sufficiently large number of particles should be analyzed to ensure sufficient statistics.

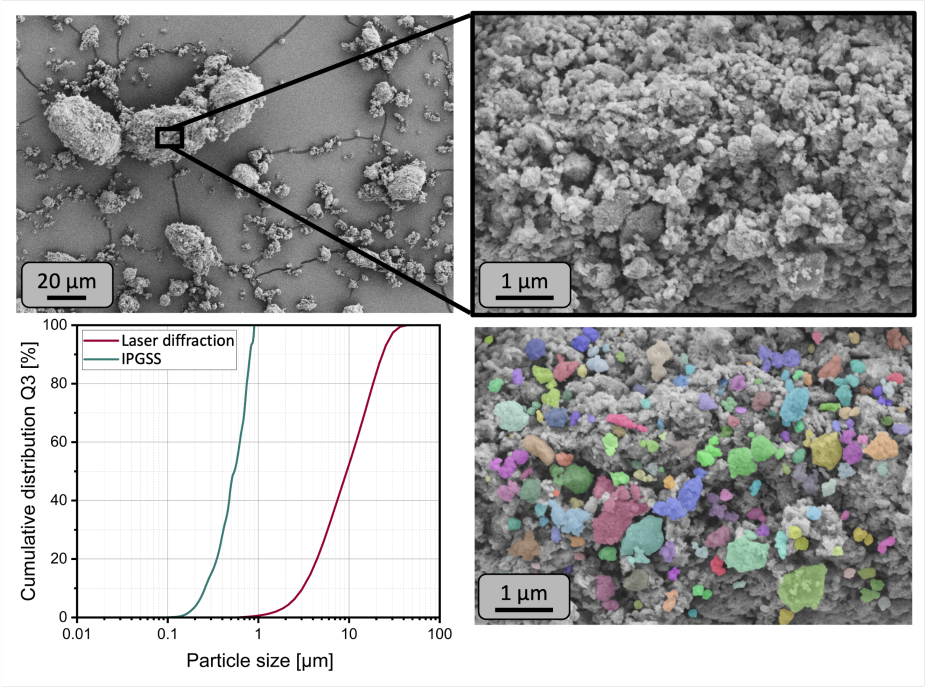

Fig. 20. Top left: SEM of comminuted LIC showing agglomerated clusters. Top right: Magnified view of one agglomerate with submicron primary particles. Bottom left: PSD from laser diffraction (red) and the IPGSS (green). Bottom right: Segmented SEM of an LIC agglomerate analyzed with the pipeline.

3.5 Discussion of Methodological Implications

Transformer Architecture and Interactive System Advantages. The SAM-based segmentation system demonstrated clear advantages over both traditional computer vision and specialized microscopy models. Extensive pre-training on over one billion masks enables zero-shot generalization, eliminating the need for domain-specific training while maintaining robust performance across diverse particle types, imaging conditions, and preparation protocols. This marks a fundamental shift from conventional approaches relying on either hand-crafted algorithms (OpenCV) or domain-specific datasets (Cellpose). SAM's transformer architecture with self-attention captures global context and long-range dependencies, supporting accurate boundary detection even under challenging conditions such as overlapping particles, varying contrast, and complex backgrounds scenarios where traditional methods consistently fail.

The IPGSS introduces a novel dimension to particle characterization by allowing user-guided analysis through prompts such as point clicks, bounding boxes, or rough sketches. This maintains transformer accuracy while enabling expert control in cases where automated algorithms underperform. In the SSB case study, this capability was

essential for isolating primary particles within agglomerates. By combining zero-shot generalization, robust boundary understanding, interactive prompting, and hierarchical filtering, the segmentation system delivers consistent performance across samples and imaging conditions. It overcomes the weaknesses of traditional methods (failure on complex images) and specialized deep learning models (merging of closely spaced particles), providing a reliable solution for both research and industrial applications.

Sample Preparation Effects and Measurement Considerations. Systematic differences between dispersed and dry preparations highlight how sample handling influences particle characterization. The smaller particle sizes observed under dispersed conditions particularly evident in D_{10} values (17.6µm vs. 42.8µm in QICPIC; 39.7–46.0µm vs. 47.3–47.6µm in segmentation system measurements), likely result from partial dissolution of aluminum oxide in aqueous media rather than agglomeration in dry samples. This interpretation is supported by a 143% increase in D_{10} but only a 2.1% increase in D_{90}, indicating selective effects on small particles with higher surface area-to-volume ratios.

Morphological parameter differences between conditions, such as broader aspect ratio and perimeter regularity distributions in dry samples, primarily reflect particle orientation on the substrate rather than intrinsic shape variation. In aqueous dispersion, however, slight surface dissolution and hydration can smooth particle edges, leading to marginally higher sphericity and a "softer" apparent shape. These effects underscore the importance of matching sample preparation to analytical goals: dry preparations preserve original size and surface features, whereas dispersed conditions enhance particle separation and boundary definition but may slightly modify surface morphology.

Validation across multiple measurement domains confirms the segmentation system's reliability for both research and industrial use. By combining transformer-based segmentation, hierarchical filtering, and depth-aware analysis, the pipeline performed reliably compared to conventional methods on complex samples while remaining compatible with established standards and reference systems. The interactive prompting capability further supports expert-guided selective analysis, and the depth-based surface characterization broadens accessibility by eliminating the need for specialized AFM instrumentation.

3D Surface Reconstruction Capabilities and Novel Measurement Scale. The depth-based surface roughness analysis provides morphological information that complements, rather than replaces, traditional techniques. By generating 3D reconstructions directly from standard SEM images, the method enables an intermediate measurement scale: it characterizes the full visible particle surface rather than the highly localized contact region measured by AFM or the boundary-limited contour captured by profile analysis. This broadens access to surface characterization by removing the need for AFM instrumentation, specialized preparation, or operator expertise, and its zero-shot capability allows rapid roughness estimation without domain-specific training data or calibration. Although the method does not aim to replicate nanoscale AFM precision,

it fills a practical gap by offering interpretable, full-surface roughness estimates using equipment already common in research and industrial settings.

The depth-derived roughness values are systematically higher than those obtained from the contour-based profile method, with an average scaling factor of approximately 3.4× (range 1.9–5.4×). This predictable amplification likely reflects the greater surface coverage inherent to the depth approach rather than methodological error, as volumetric texture across the visible hemisphere is captured rather than a single edge contour. Despite this offset, the method preserves relative roughness relationships across particles of varying composition and complexity, yielding a moderate correlation with profile measurements ($r \approx 0.64$). While this indicates room for refinement, it also confirms that the method is systematic, reproducible, and sensitive to meaningful variations in surface structure. The stable scaling factor enables straightforward calibration when absolute comparability is required, supporting use of the approach for both comparative ranking and quantitative characterization.

4 Conclusion

This work presents a comprehensive particle characterization pipeline integrating transformer-based segmentation and zero-shot depth estimation capabilities to democratize advanced microscopy analysis. The validated segmentation system addresses fundamental limitations of conventional characterization methods through application of foundation models to materials science, demonstrating good performance across size, shape, and surface roughness measurements.

The SAM-based segmentation approach achieved robust particle identification on complex samples where traditional computer vision methods systematically fail, with validation across over 20 images demonstrating consistent accuracy compared to QICPIC reference measurements from ~950,000 particles. The transformer architecture's zero-shot generalization eliminated domain-specific training requirements while outperforming both OpenCV edge-based methods that failed consistently due to the high complexity of the images and specialized Cellpose models (which showed 25-100% size overestimation). The IPGSS enables user-directed analysis through promptable segmentation, providing capabilities not available in commercial systems for specialized applications requiring selective particle identification.

Surface roughness analysis through depth-based 3D reconstruction demonstrated notable practical accessibility, enabling full-surface characterization directly from standard SEM images without the need for specialized AFM instrumentation or contact-based measurements. Validation across nine core-shell microparticles showed a moderate correlation ($r \approx 0.64$) with traditional profile-derived roughness values, alongside a systematic 3.4× overestimation that reflects the DRCS's more comprehensive hemisphere-scale sampling compared to boundary-based or localized techniques. This

broader measurement scale captures volumetric surface features that may be more representative of functional particle properties, while substantially reducing instrumentation requirements, operator expertise, and measurement time.

The SSB application exemplified practical impact, successfully resolving submicron primary particles (D_{50}=0.54μm) within agglomerated solid electrolyte structures that conventional laser diffraction measured as 9.47μm agglomerates a 17.5-fold difference critical for electrode microstructure design. The interactive segmentation enabled expert-guided analysis identifying approximately 150 individual particles within single agglomerates, demonstrating capabilities essential for advanced materials processing where particle-level information determines performance.

The hierarchical filtering strategy combining transformer confidence scoring with microscopy-specific algorithms ensured measurement reliability across diverse conditions, while maintaining compatibility with ISO standards and commercial QICPIC systems. The pipeline achieved measurement precision suitable for both research applications and industrial quality control, with low coefficients of variation for size measurements and good repeatability for morphological parameters.

Future development should focus on calibration protocols reconciling depth-based measurements with traditional surface roughness standards, computational optimization for high-throughput industrial implementation, and extension to non-spherical particle geometries through adaptive scaling. The demonstrated integration of foundation models with domain-specific algorithms establishes a framework for applying artificial intelligence to accelerate materials characterization, potentially transforming particle analysis from specialized laboratory techniques to accessible tools enabling broader scientific advancement.

The work represents the first application of promptable transformer segmentation to particle characterization, the first demonstration of hemisphere-scale depth-based surface roughness analysis from standard SEM images, and the first comprehensive validation demonstrating good performance versus conventional methods across multiple characterization domains. To facilitate broader adoption and enable researchers to apply these methods to their own materials, an accessible implementation featuring IPGSS with morphological parameter measurement is provided through an intuitive Python-based graphical interface.

Code Availability: A partial version of the interactive particle characterization tool featuring SAM-based segmentation and morphological analysis developed in this study is available as open-source software at https://github.com/ahmedeisa2. The implementation provides a user-friendly graphical interface enabling researchers to apply promptable segmentation and quantitative particle analysis to their microscopy images.

References

1. Allen, T.: Particle Size Measurement, 5th edn. Chapman and Hall, London (1997)

2. Merkus, H.G.: Particle Size Measurements: Fundamentals, Practice, Quality. Springer, Dordrecht (2009)
3. Rawle, A.: Basic Principles of Particle Size Analysis. Malvern Instruments Technical Paper (2008)
4. Eshel, G., Levy, G.J., Mingelgrin, U., Singer, M.J.: Critical Evaluation of the Use of Laser Diffraction for Particle-Size Distribution Analysis. Soil Science Society of America Journal 68(3), 736-743 (2004)
5. Xu, R., Di Guida, O.A.: Comparison of sizing small particles using different technologies. Powder Technology 132(2-3), 145-153 (2003)
6. De Boer, G.B.J., de Weerd, C., Thoenes, D., Goossens, H.W.J.: Laser Diffraction Spectrometry: Fraunhofer Diffraction Versus Mie Scattering. Particle & Particle Systems Characterization 4(1-4), 14-19 (1987)
7. Pirard, E., Lebichot, S., Krier, W.: Particle texture analysis using polarized light imaging and grey level intercepts. International Journal of Mineral Processing 84(1-4), 299-309 (2007)
8. Igathinathane, C., Pordesimo, L.O., Columbus, E.P., Batchelor, W.D., Methuku, S.R.: Shape identification and particles size distribution from basic shape parameters using ImageJ. Computers and Electronics in Agriculture 63(2), 168-182 (2008)
9. Haralick, R.M., Shapiro, L.G.: Computer and Robot Vision, vol. 1. Addison-Wesley, Reading (1992)
10. Serra, J.: Image Analysis and Mathematical Morphology. Academic Press, London (1982)
11. Otsu, N.: A Threshold Selection Method from Gray-Level Histograms. IEEE Transactions on Systems, Man, and Cybernetics 9(1), 62-66 (1979)
12. Canny, J.: A Computational Approach to Edge Detection. IEEE Transactions on Pattern Analysis and Machine Intelligence 8(6), 679-698 (1986)
13. Vincent, L., Soille, P.: Watersheds in Digital Spaces: An Efficient Algorithm Based on Immersion Simulations. IEEE Transactions on Pattern Analysis and Machine Intelligence 13(6), 583-598 (1991)
14. Meyer, F., Beucher, S.: Morphological segmentation. Journal of Visual Communication and Image Representation 1(1), 21-46 (1990)
15. LeCun, Y., Bengio, Y., Hinton, G.: Deep learning. Nature 521(7553), 436-444 (2015)
16. Krizhevsky, A., Sutskever, I., Hinton, G.E.: ImageNet Classification with Deep Convolutional Neural Networks. In: Advances in Neural Information Processing Systems, pp. 1097-1105 (2012)
17. Ronneberger, O., Fischer, P., Brox, T.: U-Net: Convolutional Networks for Biomedical Image Segmentation. In: International Conference on Medical Image Computing and Computer-Assisted Intervention, pp. 234-241. Springer (2015)
18. He, K., Gkioxari, G., Dollár, P., Girshick, R.: Mask R-CNN. In: IEEE International Conference on Computer Vision, pp. 2961-2969 (2017)
19. Falk, T., Mai, D., Bensch, R., Çiçek, Ö., Abdulkadir, A., Marrakchi, Y., Böhm, A., Deubner, J., Jäckel, Z., Seiwald, K., Dovzhenko, A., Tietz, O., Dal Bosco, C., Walsh, S., Saltukoglu, D., Tay, T.L., Prinz, M., Palme, K., Simons, M., Diester, I., Brox, T., Ronneberger, O.: U-Net: deep learning for cell counting, detection, and morphometry. Nature Methods 16(1), 67-70 (2019)
20. Caicedo, J.C., Goodman, A., Karhohs, K.W., Cimini, B.A., Ackerman, J., Haghighi, M., Heng, C., Becker, T., Doan, M., McQuin, C., Rohban, M., Singh, S., Carpenter, A.E.: Nucleus segmentation across imaging experiments: the 2018 Data Science Bowl. Nature Methods 16(12), 1247-1253 (2019)

21. Stringer, C., Wang, T., Michaelos, M., Pachitariu, M.: Cellpose: a generalist algorithm for cellular segmentation. Nature Methods 18(1), 100-106 (2021)
22. Litjens, G., Kooi, T., Bejnordi, B.E., Setio, A.A.A., Ciompi, F., Ghafoorian, M., van der Laak, J.A., van Ginneken, B., Sánchez, C.I.: A survey on deep learning in medical image analysis. Medical Image Analysis 42, 60-88 (2017)
23. Shen, D., Wu, G., Suk, H.I.: Deep Learning in Medical Image Analysis. Annual Review of Biomedical Engineering 19, 221-248 (2017)
24. Yosinski, J., Clune, J., Bengio, Y., Lipson, H.: How transferable are features in deep neural networks? In: Advances in Neural Information Processing Systems, pp. 3320-3328 (2014)
25. Pan, S.J., Yang, Q.: A Survey on Transfer Learning. IEEE Transactions on Knowledge and Data Engineering 22(10), 1345-1359 (2010)
26. Bommasani, R., Hudson, D.A., Adeli, E., Altman, R., Arora, S., von Arx, S., Bernstein, M.S., Bohg, J., Bosselut, A., Brunskill, E., et al.: On the Opportunities and Risks of Foundation Models. arXiv preprint arXiv:2108.07258 (2021)
27. Radford, A., Kim, J.W., Hallacy, C., Ramesh, A., Goh, G., Agarwal, S., Sastry, G., Askell, A., Mishkin, P., Clark, J., Krueger, G., Sutskever, I.: Learning Transferable Visual Models From Natural Language Supervision. In: International Conference on Machine Learning, pp. 8748-8763 (2021)
28. Kirillov, A., Mintun, E., Ravi, N., Mao, H., Rolland, C., Gustafson, L., Xiao, T., Whitehead, S., Berg, A.C., Lo, W.Y., Dollár, P., Girshick, R.: Segment Anything. In: IEEE International Conference on Computer Vision, pp. 4015-4026 (2023)
29. Vaswani, A., Shazeer, N., Parmar, N., Uszkoreit, J., Jones, L., Gomez, A.N., Kaiser, Ł., Polosukhin, I.: Attention is All You Need. In: Advances in Neural Information Processing Systems, pp. 5998-6008 (2017)
30. Dosovitskiy, A., Beyer, L., Kolesnikov, A., Weissenborn, D., Zhai, X., Unterthiner, T., Dehghani, M., Minderer, M., Heigold, G., Gelly, S., Uszkoreit, J., Houlsby, N.: An Image is Worth 16x16 Words: Transformers for Image Recognition at Scale. In: International Conference on Learning Representations (2021)
31. Gadelmawla, E.S., Koura, M.M., Maksoud, T.M.A., Elewa, I.M., Soliman, H.H.: Roughness parameters. Journal of Materials Processing Technology 123(1), 133-145 (2002)
32. Whitehouse, D.J.: Surfaces and their Measurement. Hermes Penton Science, London (2002)
33. Binnig, G., Quate, C.F., Gerber, C.: Atomic Force Microscope. Physical Review Letters 56(9), 930-933 (1986)
34. Eaton, P., West, P.: Atomic Force Microscopy. Oxford University Press, Oxford (2010)
35. Magonov, S.N., Whangbo, M.H.: Surface Analysis with STM and AFM: Experimental and Theoretical Aspects of Image Analysis. VCH Publishers, New York (1996)
36. Hülagü, D., Tobias, C., Dao, R., Komarov, P., Rurack, K., Hodoroaba, V.D.: Towards 3D determination of the surface roughness of core-shell microparticles as a routine quality control procedure by scanning electron microscopy. Scientific Reports 14, 17936 (2024)
37. Mandelbrot, B.B.: How Long Is the Coast of Britain? Statistical Self-Similarity and Fractional Dimension. Science 156(3775), 636-638 (1967)
38. Eigen, D., Puhrsch, C., Fergus, R.: Depth Map Prediction from a Single Image using a Multi-Scale Deep Network. In: Advances in Neural Information Processing Systems, pp. 2366-2374 (2014)
39. Godard, C., Mac Aodha, O., Firman, M., Brostow, G.J.: Digging Into Self-Supervised Monocular Depth Estimation. In: IEEE International Conference on Computer Vision, pp. 3828-3838 (2019)
40. Ranftl, R., Bochkovskiy, A., Koltun, V.: Vision Transformers for Dense Prediction. In: IEEE International Conference on Computer Vision, pp. 12179-12188 (2021)

41. Ranftl, R., Lasinger, K., Hafner, D., Schindler, K., Koltun, V.: Towards Robust Monocular Depth Estimation: Mixing Datasets for Zero-shot Cross-dataset Transfer. IEEE Transactions on Pattern Analysis and Machine Intelligence 44(3), 1623-1637 (2022)
42. Bhat, S.F., Alhashim, I., Wonka, P.: AdaBins: Depth Estimation Using Adaptive Bins. In: IEEE Conference on Computer Vision and Pattern Recognition, pp. 4009-4018 (2021)
43. Yin, W., Liu, Y., Shen, C., Yan, Y.: Enforcing Geometric Constraints of Virtual Normal for Depth Prediction. In: IEEE International Conference on Computer Vision, pp. 5684-5693 (2019)
44. Long, J., Shelhamer, E., Darrell, T.: Fully Convolutional Networks for Semantic Segmentation. In: IEEE Conference on Computer Vision and Pattern Recognition, pp. 3431-3440 (2015)
45. Chen, L.C., Papandreou, G., Kokkinos, I., Murphy, K., Yuille, A.L.: DeepLab: Semantic Image Segmentation with Deep Convolutional Nets, Atrous Convolution, and Fully Connected CRFs. IEEE Transactions on Pattern Analysis and Machine Intelligence 40(4), 834-848 (2018)
46. ISO 4287:1997: Geometrical Product Specifications (GPS) - Surface texture: Profile method - Terms, definitions and surface texture parameters. International Organization for Standardization, Geneva (1997)
47. ISO 4288:1996: Geometrical Product Specifications (GPS) - Surface texture: Profile method - Rules and procedures for the assessment of surface texture. International Organization for Standardization, Geneva (1996)
48. Sympatec GmbH: QICPIC - Dynamic Image Analysis. Technical Documentation (2020)
49. ISO 13322-2:2006: Particle size analysis - Image analysis methods - Part 2: Dynamic image analysis methods. International Organization for Standardization, Geneva (2006)
50. Bradski, G.: The OpenCV Library. Dr. Dobb's Journal of Software Tools 25, 120-125 (2000)
51. Janek, J., Zeier, W.G.: A solid future for battery development. Nature Energy 1, 16141 (2016)
52. Randau, S., Weber, D.A., Kötz, O., Koerver, R., Braun, P., Weber, A., Ivers-Tiffée, E., Adermann, T., Kulisch, J., Zeier, W.G., Richter, F.H., Janek, J.: Benchmarking the performance of all-solid-state lithium batteries. Nature Energy 5, 259-270 (2020)
53. ISO 13322-1:2014: Particle size analysis - Image analysis methods - Part 1: Static image analysis methods. International Organization for Standardization, Geneva (2014)
54. ISO 9276-6:2008: Representation of results of particle size analysis - Part 6: Descriptive and quantitative representation of particle shape and morphology. International Organization for Standardization, Geneva (2008)
55. DIN 66141:1974: Representation of grain size analysis; RRSB-grid. Deutsches Institut für Normung, Berlin (1974)
56. Frankenberg, F., Heck, C.A., Kissel, M., Lange, M.A., Faka, V., Diener, A., Haase, P., Michalowski, P., Zeier, W.G., Janek, J., Kwade, A.: Tailoring composite microstructure through milling for dry-processed sulfide-based solid-state battery cathodes. Small (2025).
57. Tinke, A.P., Govoreanu, R., Weuts, I., Vanhoutte, K., De Smaele, D.: A review of underlying fundamentals in a wet dispersion size analysis of powders. Powder Technology 196(2), 102–114 (2009).
58. Jaffari, S., Forbes, B., Collins, E., Barlow, D., Martin, G.P., Murnane, D.: Rapid characterisation of the inherent dispersibility of respirable powders using dry dispersion laser diffraction. *International Journal of Pharmaceutics* **447**(1–2), 124–131 (2013).
59. Ruhl, J., Riegger, L.M., Ghidiu, M., Zeier, W.G.: Impact of solvent treatment of the superionic argyrodite Li_6PS_5Cl on solid-state battery performance. *Advanced Energy and Sustainability Research* **2**(2), 2000077 (2021).

60. Tron, A., Paolella, A., Beutl, A.: New insights of infiltration process of argyrodite Li_6PS_5Cl solid electrolyte into conventional lithium-ion electrodes for solid-state batteries. Batteries 9(10), 503 (2023).
61. Shi, T., Tu, Q., Tian, Y., Xiao, Y., Miara, L.J., Kononova, O., Ceder, G.: High active material loading in all-solid-state battery electrode via particle size optimization. Advanced Energy Materials 10(1), 1902881 (2020).
62. Frankenberg, F., Kissel, M., Burmeister, C.F., Lippke, M., Janek, J., Kwade, A.: Investigating the production of all-solid-state battery composite cathodes by numerical simulation of the stressing conditions in a high-intensity mixer. Powder Technology 435, 119403 (2024).
63. Clausnitzer, M., Mücke, R., Al-Jaljouli, F., Hein, S., Finsterbusch, M., Danner, T., Rattakhova-Rohlfing, D., Guillon, O., Latz, A.: Optimizing the composite cathode microstructure in all-solid-state batteries by structure-resolved simulations. Batteries & Supercaps 6(11), e202300167 (2023).